Reaction Chemistry & Engineering

PAPER

View Article Online
View Journal | View Issue

Cite this: *React. Chem. Eng.*, 2018, **3**, 826

Bubble formation in catalyst pores; curse or blessing?†

Roger Brunet Espinosa,‡[a] Michel H. G. Duits,[b] Daniel Wijnperlé,[b] Frieder Mugele [b] and Leon Lefferts *[a]

Received 20th June 2018,
Accepted 14th September 2018

DOI: 10.1039/c8re00110c

rsc.li/reaction-engineering

H_2O_2 decomposition experiments on Pt were performed in a glass microreactor, simulating arrays of catalyst pores. The formation of bubbles inside the model nanopores was observed with an optical microscope. It was found that the bubble initiation time strongly depends on the diffusion length and the H_2O_2 concentration. The amount of catalyst did not have a significant effect, suggesting that the reaction is diffusion limited. Results show that bubble formation can decrease the reaction rate by physically blocking the active sites, but also can accelerate the reaction by creating a forced convective flow inside the nanochannels due to bubble migration. Similar behaviour is likely to occur in a real catalyst and thus, a smart design of the catalytic support could be used to enhance reaction rates.

Introduction

Heterogeneous catalysis is truly multidisciplinary, merging the fields of physics and chemistry. Most processes in the chemical industry make use of heterogeneous catalysts in the production of chemicals and fuels, in order to maximize production capacity as well as efficiency and selectivity of processes. Over the last decades, advanced techniques have been developed to gain new insights into the fundamentals of catalysis including reaction mechanisms. Chemical processes on the surface of catalysts, as well as the influence of the surface structure are increasingly understood based on studies using 2D model catalysts. More recently, similar information is becoming available also for more practical catalysts with significant surface area.[1,2] However, there is still an important lack of understanding of the transport processes occurring inside catalyst pores as direct observations are generally not available.

As described by Thiele[3] and Zeldovich[4] in 1939, a reaction inside a catalyst pore combines diffusion of the reactants and products, as described *e.g.* by Fick's law, and the catalytic reaction on the active sites supported on the pore wall. It is assumed that the liquid inside the catalyst pores remains stagnant, implying that transport of reactants and products proceeds exclusively *via* slow molecular diffusion between the pore mouth and the active sites deeper in the pore, leading to decreased reactant concentration at the active sites and thus, low reaction rate.[5–8]

However, the Thiele/Zeldovich description does not apply for the chemical reactions where an important amount of gas or heat is generated and cannot be removed *via* diffusion or thermal conduction respectively.[9–18] In these cases, gas or vapour bubbles may be generated if the partial pressure of gas or vapour exceeds the maximum pressure in the pores. These bubbles grow and displace the liquid inside the pore towards the bulk of the reactor. Once a bubble reaches the pore mouth, the pressure of the bubble equilibrates with the pressure of the reactor, dragging new liquid into the pore.[10–12,16] This creates a chaotic movement of the liquid inside the pore network of the catalyst; velocities up to 100 m s^{-1} are claimed.[10–12] This behaviour was named the 'oscillation theory' by Datsevich and has not yet been confirmed independently.[11]

One of the most remarkable consequences of this oscillatory movement is the enhancement of the external (500-fold increase)[9–12,16] and internal mass transport (mainly in the outer shell of the catalyst particles).[9,10,12] Other peculiarities are the notorious increase in the temperature difference between the centre and the surface of the catalyst (almost one order of magnitude higher than predicted by the Thiele/Zeldovich model)[12,13] and the change in apparent reaction orders.[11,12] However, this chaotic movement of the liquid only happens near the pore mouth, leading to stagnant zones in the deeper parts of the pores, where the reaction is

[a] *Catalytic Processes and Materials, Faculty of Science and Technology, MESA+ Institute for Nanotechnology, University of Twente, P.O. Box 217, 7500 AE Enschede, Netherlands. E-mail: l.lefferts@utwente.nl*
[b] *Physics of Complex Fluids, Faculty of Science and Technology, MESA+ Institute for Nanotechnology, University of Twente, P.O. Box 217, 7500 AE Enschede, Netherlands*

† Electronic supplementary information (ESI) available. See DOI: 10.1039/c8re00110c

‡ Present address: Beele Engineering, Vierde Broekdijk 12, 7122JD, Aalten, Netherlands.

suppressed.[12] Furthermore, it can also damage the catalyst due to cavitation in the pores.[16]

These concepts have been indirectly inferred experimentally based on kinetic data but direct observation of gas bubbles and liquid motion inside the pores is still lacking. In this work we study the catalytic decomposition of hydrogen peroxide (H_2O_2) on Pt in a glass chip that models an array of catalyst pores. H_2O_2 decomposition was chosen as model reaction since it is a fast reaction in aqueous phase, forming a gaseous product (O_2) without any side reactions.[18,19] For the first time, to the best of our knowledge, a microfluidic device is used to study the effect of internal mass transfer *via* formation and behaviour of bubbles, directly with an optical microscope. The study reports on the effect of the geometry of the nanochannel, the amount of catalyst and the H_2O_2 concentration on the formation of bubbles and the impact of those on the reaction rate.

Experimental

Chip fabrication

The nano- and microfluidic channels as presented in Fig. 1, were fabricated on two separate substrates and then bonded. The bottom substrate (Fig. 2A) contains the nanochannels, which have a Pt patch on the bottom. The top substrate (Fig. 2B) contains the microchannels and the access holes.

A <100> silicon wafer (Fig. 2A-1) was thermally oxidized to obtain a layer of 450 nm SiO_2 (Fig. 2A-2). This thickness defines the depth of the nanochannels. Nanochannels were then patterned by UV lithography and the exposed SiO_2 was etched in a buffered hydrofluoric acid (BHF) solution composed of hydrofluoric acid (HF) and ammonium fluorite (NH_4F) until the silicon surface was reached (Fig. 2A-3). A second UV lithography step was performed to create the catalyst patch area (Fig. 2A-4). Afterwards, a layer of Ti/Pt was deposited by sputtering (Fig. 2A-5). The excess metal was removed by a lift-off process (Fig. 2A-6).

The top substrate consists of a 500 μm thick borofloat glass wafer (Fig. 2B-1). A Cr/Au layer was deposited to act as an etching mask during the glass etching process (Fig. 2B-2). Next, the microchannel pattern was defined and the wafer was etched in 25% HF solution to create 100 μm deep microchannels (Fig. 2B-3). Through holes were made from the back side of the wafer by powder blasting with 29 μm diameter alumina grit (Fig. 2B-5).

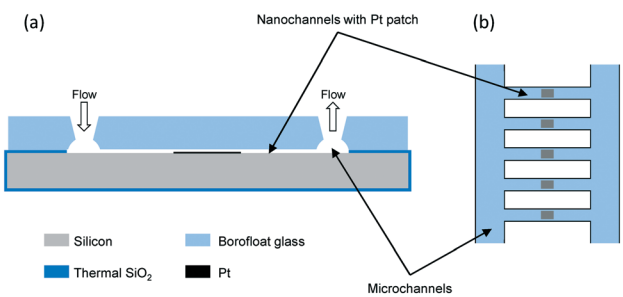

Fig. 1 a) Cross-sectional and b) top view of the chip.

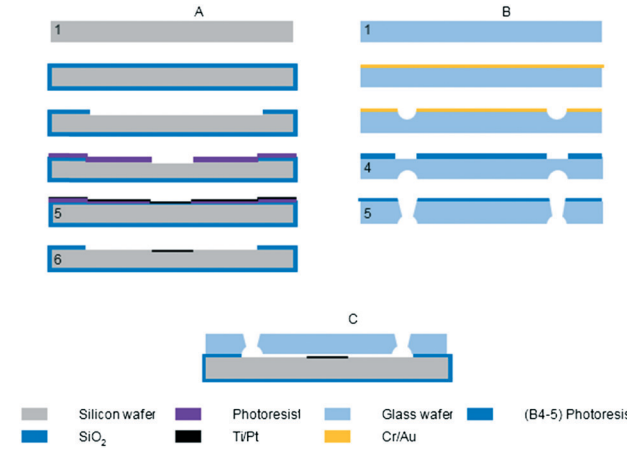

Fig. 2 Schematic description of the fabrication steps of the chip steps A, B and C are described in detail in the text.

Both substrates were cleaned thoroughly, aligned and pressed together (Fig. 2C). Finally, the stack was annealed and bonded together in a furnace at 450 °C. The resulting chip is shown in Fig. 3a.

Description of the chip

The fabricated chip (Fig. 3a) consists of two symmetric meandering microchannels interconnected with an array of 96 parallel nanochannels varying in width, length and amount of catalyst. The shortest nanochannels are positioned in the centre of the chip. The other nanochannels are distributed symmetrically at both sides of the shortest nanochannels except for the longest set of nanochannels, which are only present at one side. The different nanochannel lengths are 2900, 8500 and 14 000 μm. Please note that Fig. 3a also shows channels 20 000 and 25 000 μm long, which have not been used in this study. For every length there are four different widths: 10, 30, 50 and 70 μm (Fig. 3b). For every width there are three different Pt sizes, varying in length (35, 250 and 3140 μm). All Pt patches have a height of 10 nm and a width 4 μm narrower than the nanochannel. The shortest nanochannels have shorter Pt lengths (35, 180 and 250 μm). For a full overview of all dimensions of

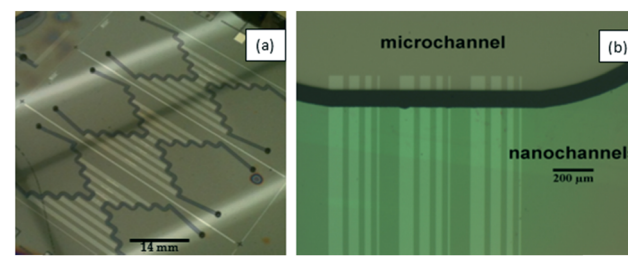

Fig. 3 a) Picture of the final device prior to dicing, b) optical microscope image of the microchannels substrate aligned and fusion bonded to the nanochannels substrate.

the nanochannels used in this work, and the Pt catalysts, see Table S1 in ESI.†

Catalytic tests

MilliQ water contained in a glass bottle was degassed with a commercial in-line degasser (Perkin Elmer, PE200) to remove any traces of gas. Next, the water was introduced into the chip which was placed in a metallic holder (Micronit® Fluidic Connect Pro). The water flow was generated *via* a hydrostatic pressure of 40 mbar. The water was first directed to one of the microchannels and then to the other *via* a PEEK tubing that connected both microchannels in series. The nanochannels were filled by capillarity. After 24 h flowing water through the chip to ensure complete filling, one of the microchannels was bypassed and closed, keeping water flow only through one microchannel. Next, water was replaced by a H_2O_2 solution, as shown in Fig. 4. The experiments were designed in this way to supply H_2O_2 to the catalyst *via* molecular diffusion exclusively, ensuring the liquid in the nanochannels is stagnant. Co-feeding H_2O_2 *via* both microchannels in parallel or connecting both microchannels in series resulted in some convection inside the nanochannels.

Experiments were all performed at room temperature with different H_2O_2 concentrations (0, 0.04, 0.13, 0.64, 1.49 and 2.35 mole per L). A microscope (Nikon, Eclipse L150) equipped with a camera (PCO Pixelfly) was positioned above the chip to record formation of any bubbles. The amount of O_2 formed was estimated from the volume of the bubbles.

Model

Molecular diffusion fluxes of H_2O_2 and O_2 were calculated based on eqn (1), assuming no transport due to convection.

$$J = -D \times \frac{\Delta C}{\Delta l} \quad (1)$$

where J is the diffusion flux in mol s^{-1} m^{-2}, D is the diffusion coefficient of H_2O_2 (9.8×10^{-10} m^2 s^{-1} (ref. 20)) or O_2 (2.0×10^{-9} m^2 s^{-1} (ref. 21)) in water, ΔC the difference in concentration at the centre of the pore and at the pore mouth for H_2O_2 or O_2 in mol m^{-3} and Δl the diffusion length in m.

The rate constant of H_2O_2 decomposition can be estimated with eqn (2).

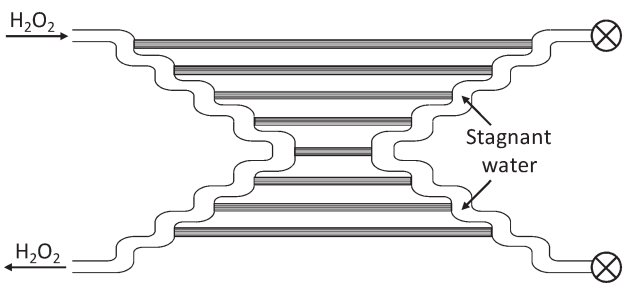

Fig. 4 Flow operation of the chip during reaction.

$$R = k \times [H_2O_2]^{\alpha} \times (W_{Pt} \times L_{Pt}) \quad (2)$$

where R is the reaction rate in mole per s m^{-3}, k the rate constant in s^{-1} m^{-2}, $[H_2O_2]$ the concentration of H_2O_2 in mole per m^3, α, the reaction order (assumed 1) 18, W_{Pt} and L_{Pt} the width and the length of the Pt patch respectively, both in m.

The experimental value of R can be estimated based on the rate of formation of O_2. The number of moles of O_2 formed is calculated using the ideal gas law based on the volume of the O_2 bubbles. The volume of these bubbles is estimated as the product of the axial cross-sectional area of the bubble and the height (450 nm) of the nanochannel. Note that this approach neglects both the curvature of the bubble (an overestimation) and the flux of O_2 in the dissolved state (an underestimation). The temperature is 20 °C, whereas the pressure is the ambient value (1 bar) augmented with the Laplace pressure according eqn (3).

$$\Delta P = \gamma \times \left(\frac{1}{R_1} + \frac{1}{R_2} \right) \quad (3)$$

Here ΔP is the Laplace pressure in Pa, γ is the surface tension (0.072 N m^{-1} for pure water) and R_1 and R_2 the two radii of curvature of the bubble in m. Considering R_1 and R_2 equal to the half of the height (450 nm) and the width (10–70 μm) of the nanochannels respectively, then, $1/R_2$ will always be negligible. Consequently, the bubbles will have the same pressure (approximately 4.2 bar) in all nanochannels.

The maximum O_2 concentration in the liquid inside the nanochannel is determined by the Henry's law (eqn (4)):

$$[O_2] = H_{O_2} \times (P_{reactor} + \Delta P) \quad (4)$$

where $P_{reactor}$ is the pressure in the microchannel (1 bar) and H_{O_2} is the Henry's coefficient for pure O_2 in water (1.3×10^{-5} mole per m^3 bar^{-1}).[22]

Results

As described above, the experiments are initiated by flushing H_2O_2 solutions through one of the microchannels. Subsequently, the central region of the nanochannels with the Pt patches is continuously monitored with a CCD camera. For H_2O_2 concentrations of 0.64 mole per L and higher, bubbles appeared after an induction time varying between 10 and 200 minutes, depending on the concentration and the length of the nanochannel. For the two lowest concentrations of H_2O_2 (0.04 and 0.13 mole per L) no bubble formation was observed within 5 h of reaction time. Fig. 5 shows a typical example of bubble formation. The Pt patches appear as highly reflective bright areas in the middle of each channel; bubbles appear as regions of intermediate grey levels. Water-filled parts of the channels appear as dark grey with little contrast to the adjacent channel walls. Note that the bubbles appear primarily as grey rectangles filling the entire width of the channels and that most bubbles in the figure have already

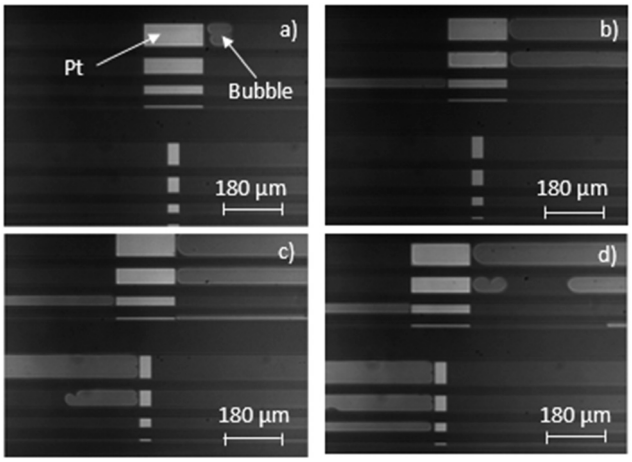

Fig. 5 Bubble formation in the shortest nanochannels (2900 μm), with two different platinum lengths (35 and 180 μm) and four different widths (10, 30, 50 and 70 μm) using 0.64 mole H_2O_2 per L after a) 1 h 18 min, b) 1 h 35 min, c) 1 h 45 min, d) 1 h 53 min.

grown to be longer than the width of the field of view of the figure. The H_2O_2-rich microchannel is on the left, the stagnant water filled microchannel is on the right.

Fig. 6a and b show the effect of the diffusion length (distance from the microchannel to the Pt front) on the time needed to initiate bubble formation for the experiments performed with 0.64 and 1.49 mole H_2O_2 per L. It reveals that bubble initiation time increases with the diffusion length. This is also observed for different nanochannel widths (not shown here). Fig. 6a and b also show that the length of the Pt patch has no significant effect on the bubble initiation time. The only exception is the shortest Pt length (35 μm) for the experiment with 0.64 mole H_2O_2 per L, which exhibits longer initiation times than the other Pt lengths (Fig. 6a). A very similar trend is found for a smaller nanochannel width (Fig. S1 in ESI†).

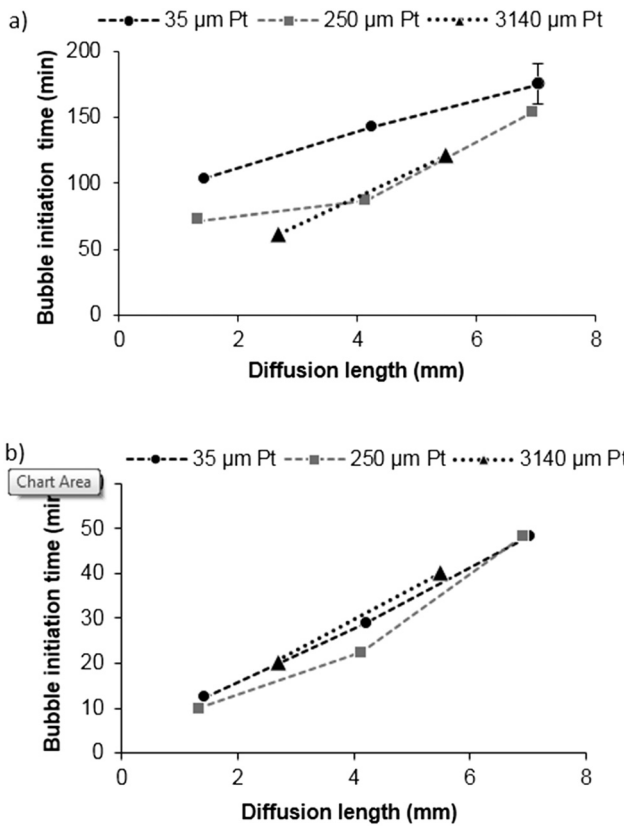

Fig. 6 Effect of the diffusion length and the Pt length on the bubble initiation time for a constant nanochannel width of 70 μm and different Pt lengths (35, 250 and 3140 μm). The experiments were performed with a) 0.64 mole H_2O_2 per L, b) 1.49 mole H_2O_2 per L.

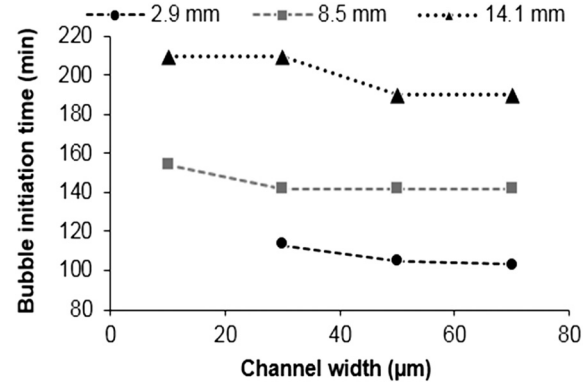

Fig. 7 Effect of the nanochannel width on the bubble initiation time for a constant Pt patch length of 35 μm and different nanochannel lengths (2.9, 8.5 and 14 mm). The experiment was performed with 0.64 mole H_2O_2 per L.

Fig. 7 shows a very weak effect of the nanochannel width on the bubble initiation time for the experiment performed with 0.64 mole H_2O_2 per L. Clearly, the diffusion length has a much stronger effect, in agreement with Fig. 6. For narrower nanochannels, the bubble initiation time is slightly longer. This effect was observed independently of the amount of Pt and the H_2O_2 concentration (not shown).

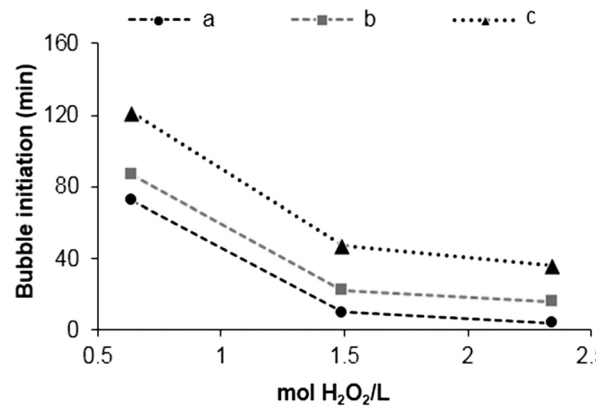

Fig. 8 Effect of the H_2O_2 concentration on the bubble initiation time for 70 μm wide nanochannels, a) 2.9 mm nanochannel length and 250 μm Pt patch length; b) 8.5 mm nanochannel length and 250 μm Pt patch length; c) 14 mm nanochannel length and 3140 μm Pt patch length.

Fig. 8 shows that bubble formation occurs faster at higher H_2O_2 concentrations. At concentrations below 0.13 mole H_2O_2 per L, no bubbles were observed within 5 hours of experiment. For the concentrations 0.64, 1.49 and 2.35 mole H_2O_2 per L, all nanochannels showed bubbles and presented similar trends in bubble initiation time.

The bubbles always nucleate on the Pt patch. Fig. 9 shows as a typical example that the subsequent bubble growth can occur in both directions *i.e.*, towards the microchannel filled with stagnant water as well as towards the microchannel filled with the H_2O_2 solution. The direction in which bubbles start to grow, appears to be random: the number of bubbles growing towards the H_2O_2 microchannel (46%) is almost the same as the number growing towards the water microchannel (48%), whereas a small fraction of bubbles grow in both directions simultaneously (6%). This random-like behaviour is found regardless of the pore geometry, Pt amount and H_2O_2 concentration.

Fig. 10 shows that bubbles forming towards the microchannel filled with H_2O_2 have a growth rate that decreases abruptly during the initial minutes of reaction, becoming extremely low at long reaction times. The rate of formation is estimated based on the volume of the gas bubbles that are observed, as described in detail in Experimental.

In contrast, Fig. 10 also shows that when bubbles grow towards the microchannel filled with water, reaction rates are several orders of magnitude higher than when bubbles form towards the microchannel filled with H_2O_2. Furthermore, the reaction rate remains constant over more than 500 minutes of reaction. These bubbles initially form above the catalyst patch and continuously grow until the catalyst is entirely covered. Then, a part of the bubble detaches and migrates towards the H_2O filled microchannel. The bubble remaining above the Pt continues to grow and the process repeats itself. This induces convection, as illustrated by the movie in ESI.†

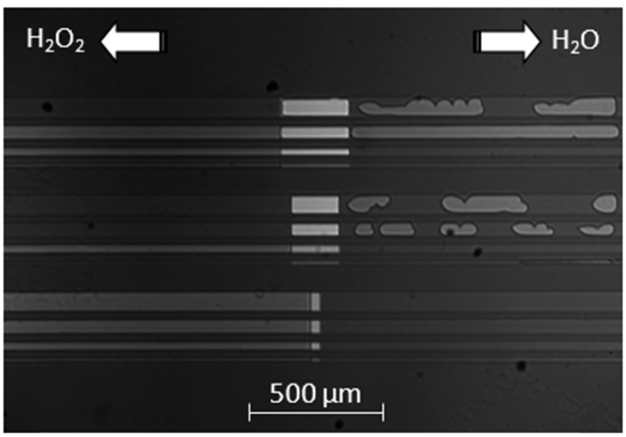

Fig. 9 Example of randomness in the direction in which bubbles grow, for nanochannels with a length of 2.9 mm after 5.5 h of experiment with a solution of 0.64 mole H_2O_2 per L.

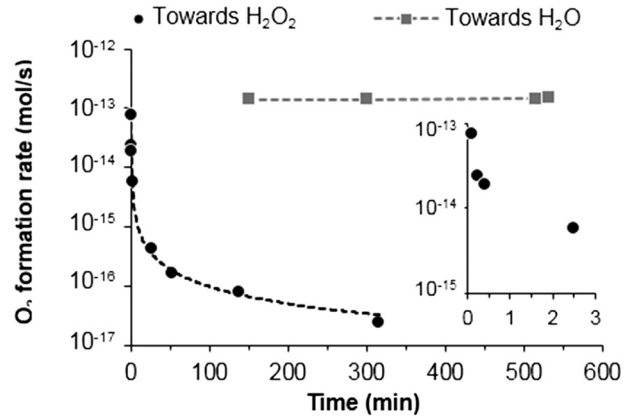

Fig. 10 Evolution of O_2 formation rate in time for two nanochannels forming bubbles towards different directions. The insert shows a zoom-in on the changes in the first few minutes. Experiment was performed with 0.64 mole H_2O_2 per L. Both nanochannels were 2.9 mm long, 50 μm wide and had Pt lengths of 35 μm (towards H_2O_2) and 180 μm (towards H_2O). Time zero is defined as the time when the first bubble is observed.

Discussion

Bubble formation

Catalytic decomposition of H_2O_2 occurs at the Pt patches deposited in the centre of the nanochannels, producing water and O_2 as the only products of the reaction (eqn (5)). Concentration profiles in the nanochannels develop in time as result of the diffusion of H_2O_2 and O_2 and the decomposition reaction, leading to a pseudo steady state. At pseudo steady state, the highest O_2 concentration in the nanochannel will occur above the Pt patch. If this O_2 concentration is higher than the O_2 saturation concentration, bubbles will form. In case of lower O_2 concentrations, no bubbles can form.

$$2H_2O_2 \xrightarrow{\text{Catalyst}} 2H_2O + O_2 \quad (5)$$

No bubbles were observed in the experiments with 0.04 and 0.13 mole H_2O_2 per L. This indicates that the maximum O_2 concentration above the Pt remained lower than 5.5 mole O_2 per m^3. This saturation concentration considers the confinement effect on the pressure (eqn (4)). Therefore, the maximum O_2 flux ($J_{O_2\ max}$) without formation of bubbles can be derived from eqn (1) ($J_{O_2\ max} = D_{O_2} \times 5.5/\Delta x$).

According to Fig. 6a (0.64 mole H_2O_2 per L), the amount of Pt has a minor effect on the bubble initiation time, especially for the medium (250 μm) and large Pt patches (3140 μm). For higher H_2O_2 concentrations (1.49 mole H_2O_2 per L), the bubble initiation time was not influenced by the amount of Pt in the nanochannel, even for the small Pt patches (Fig. 6b). Thus, the reaction is diffusion limited and bypassing of H_2O_2 over the Pt patch is negligible. Therefore, the concentration profiles of O_2 and H_2O_2 in the nanochannels can be qualitatively depicted as in Fig. 11. It is worth stressing that initially the O_2 concentration in the microchannels is negligible.

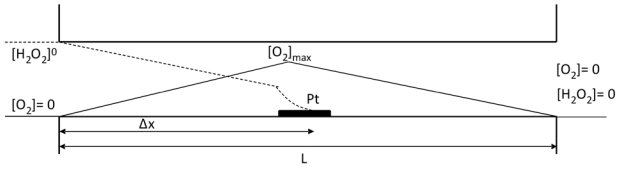

Fig. 11 Qualitative scheme of O_2 and H_2O_2 concentration profiles inside a nanochannel in case of a high reaction/diffusion rate ratio.

Since the reaction is fast and H_2O_2 reaching the Pt is completely converted to O_2 in most cases, the ratio between the H_2O_2 flux ($J_{H_2O_2} = D_{H_2O_2} \times [H_2O_2]/\Delta x$) and the maximal O_2 flux ($J_{O_2\ max}$) will determine whether bubbles will form or not above the Pt patch (eqn (6)). For ratios greater than 4 (as explained below), bubbles are expected to form while for ratios lower than 4, O_2 will stay dissolved in the liquid while diffusing out

$$\frac{0.5\times J_{H_2O_2}}{2\times J_{O_2\ max}} = \frac{D_{H_2O_2}\times\frac{\Delta[H_2O_2]}{\Delta x}\times A}{D_{O_2}\times\frac{\Delta[O_2]}{\Delta x}\times A\times 4} = \frac{D_{H_2O_2}\times[H_2O_2]}{[O_2]_{sat}\times D_{O_2}\times 4} \quad (6)$$

$D_{H_2O_2}$ and D_{O_2} are the diffusion coefficients of H_2O_2 and O_2 in water respectively, $\Delta[H_2O_2]$ and $\Delta[O_2]$ are the concentration differences (in mole per m^3), Δx is the diffusion distance (in m) and A is the diffusion area (in m^2). The ($J_{O_2\ max}$) is multiplied by a factor of two because O_2 diffuses in two directions (towards both microchannels) and the $J_{H_2O_2}$ is corrected by a factor of 0.5 because of the stoichiometry of the reaction, together responsible for the factor 4.

Table 1 shows that bubbles are expected to form at all H_2O_2 concentrations, except for 0.04 mole per L since the corresponding flux ratios are greater than 4. However, for the experiment with 0.13 mole H_2O_2 per L, no bubbles were observed experimentally. At this stage, we cannot clearly identify the origin of this deviation of the threshold concentration. Uncertainties in the manufacturing process may cause minor variations in the channel height that would affect the O_2 flux. Possibly, the flux of H_2O_2 is overestimated since molecular diffusion is considered only in one dimension and any H_2O_2 concentration gradients perpendicular above the Pt patch are ignored. Even though this could support the absence of bubbles in the experiment with 0.13 mole H_2O_2 per L, it is also possible that bubbles did not form because the experimental time (5–6 h) was too short to establish the final concentration profiles and nucleate the bubble.

Table 1 Ratio from eqn (6) for all the H_2O_2 concentrations tested

H_2O_2 concentration (mole per L)	$J_{H_2O_2}/(4\times J_{O_2\ max}$
0.04	0.9
0.13	2.9
0.64	14.5
1.49	33.7
2.35	53.1

The data in Fig. 8 indicate that the bubble initiation time depends in a nonlinear way on the H_2O_2 concentration, leading to a steeper increase as $[H_2O_2]$ gets lowered.

Notice that in eqn (6) and Fig. 11 it is implicitly assumed that the reaction is fast as compared to diffusion and consequently the formation of bubbles only depends on the H_2O_2 concentration and not on the amount of catalyst or the geometry of the nanochannel. This assumption is supported by the observation that the experiments with 0.04 and 0.13 mole H_2O_2 per L do not exhibit bubbles in any of the nanochannels while the experiments with 0.64, 1.49 and 2.35 mole H_2O_2 per L, present bubbles in all used nanochannels (see Table S1 in ESI†).

Effect of bubble direction on reaction rate

The direction in which the first formed bubble expands appears to be random, as illustrated in Fig. 5 and 9. This clearly indicates that the initial transport of H_2O_2 towards the Pt occurs only *via* molecular diffusion and not by convective flow inside the nanochannels, otherwise all bubbles would grow and move in the same direction, as indeed observed in control experiments when convective flux was not properly suppressed.

When bubbles continue to grow towards the microchannel containing H_2O_2, the rate of O_2 gas formation decreases exponentially, as shown in Fig. 10. The growth rate decreases because the presence of bubbles suppresses the supply of H_2O_2 by physically blocking the diffusion of the reactant molecules to the catalytic sites. Nevertheless, bubbles do not stop growing completely. We attribute this to the presence of a thin stagnant layer of water on the walls of the nanochannel at the position of the bubble and to the liquid gutters that typically form in two-phase flows with rectangular channels. This enables continuous yet slow transport of H_2O_2 to the Pt patch.

On the other hand, if the bubbles grow towards the microchannel with stagnant water, the O_2 formation rate remains high, even after hours of reaction (Fig. 10). The bubbles are pinned for some time to the Pt patch but then detach and move in the direction of the microchannel filled with water. The movement of these bubbles displaces liquid, which is immediately replaced by H_2O_2 solution from the other microchannel, creating convection of the liquid, as illustrated by the movie in ESI.† As result, the reaction rate is several orders of magnitude higher as compared to the case where H_2O_2 transport occurs only *via* molecular diffusion. For example, the maximum O_2 formation rate (assuming complete conversion on the Pt patch) achievable under molecular diffusion for the experiment shown in Fig. 10 (towards H_2O) would be 4.8×10^{-15} mole O_2 per s (eqn (1)). However, the experimental reaction rate is 1–2 orders of magnitude higher ($\approx 1.5 \times 10^{-13}$ mole O_2 per s). We speculate that the movement of liquid, caused by the movement of bubbles (detached from the Pt), is induced by preference of the

bubble to contact the wall of the nanochannel rather than the Pt patch. The Pt surface is covered with oxygen atoms, probably causing a more hydrophilic surface than the walls of the silica nanochannels. Consequently, bubbles migrate from the Pt to the nanochannel, decreasing the overall interfacial energy. The energy released during the reaction might also play a role in the movement of the bubbles. It can also not be ruled out that the slightly narrower height of the channel at the Pt patch, *i.e.* 440 nm *versus* 450 nm in the channel, drives the bubbles in to the channel.

The average linear velocity of the liquid is equal to the linear velocity of the bubbles inside the nanochannels since the liquid is effectively trapped between bubbles. It is calculated as the distance travelled by the bubble front in a given time. From the linear velocity of the liquid, the H_2O_2 flux to the Pt catalyst can be calculated. It can be estimated that 28% of the H_2O_2 transported to the Pt patch is converted in the nanochannel shown in Fig. 10 (towards H_2O). Details on the calculation of H_2O_2 conversion are provided in ESI.† These results confirm that the high O_2 formation rates can be explained by H_2O_2 transport *via* the convection induced by the observed bubble motion.

A calculation of the turn over frequency (TOF) using the data reported in Fig. 10 (rate: 10–13 mole per s, H_2O_2 concentration: 0.64 mole per L, room temperature) shows values of 0.5 s^{-1}. This value is in close agreement with the TOFs calculated from data in literature on Pt catalyst for H_2O_2 decomposition with similar temperature (25 °C) but lower H_2O_2 concentration (0.06 mole H_2O_2 per L), resulting in 0.5 s^{-1},[21] as well as with the TOF calculated from data in (ref. 17) (0.6 s^{-1}) at similar temperature (27 °C) and an even lower H_2O_2 concentration (0.01 mole H_2O_2 per L). This clearly proves that the data estimated here result in reasonable TOFs.

Bubble initiation time

The experimental results demonstrate that bubble initiation time is strongly affected by the diffusion length (Fig. 6) and the concentration of H_2O_2 in the feed stream (Fig. 8). All these parameters influence the diffusion fluxes of H_2O_2 and O_2 (eqn (1)) and/or the kinetics of the reaction (eqn (2)).

The diffusion flux is inversely proportional to the diffusion distance (eqn (1)). Consequently, long diffusion distances will slow down the transport of H_2O_2 to the catalyst and the transport of O_2 to the microchannels. In this case, longer times will be needed to fully develop the concentration profiles inside the nanochannels and consequently, the time of bubble formation will be increased, as shown in Fig. 6. As mentioned in section 3.1, the diffusion distance will not determine the formation of bubbles (eqn (6)) but only the time needed for bubble nucleation to occur.

Increasing the H_2O_2 concentration accelerates bubble nucleation (Fig. 8), *via* increasing the H_2O_2 diffusion flux (eqn (1)) and the reaction rate (eqn (2)). Even though the reaction is exothermic (ΔH = −98.2 kJ per mole (ref. 18)), a significant increase in temperature is not to be expected. The adiabatic temperature rise of the liquid above the Pt surface (calculated from the reaction enthalpy and the heat capacity of water) for the experiment with 0.64 mole H_2O_2 per L, was estimated between 3.5 and 6 °C, depending on the nanochannel. The actual temperature rise will be significantly smaller because the calculation does not consider dissipation of heat *via* the Pt patch to the SiO_2 substrate. This is qualitatively in agreement with the results reported by Datsevich *et al.*[18] who observed temperature changes in the order of 1 °C.

The width of the nanochannel does not influence the transport of H_2O_2 and O_2 since the diffusion flux is independent of the area of diffusion. However, Fig. 7 shows a small increase in the time of bubble formation for the narrowest nanochannels. This phenomenon occurs because the amount of Pt does not scale with the width of the nanochannel. The distance between the Pt patch and side walls of the nanochannels is always 2 μm, therefore, narrow nanochannels contain relatively less Pt than wide nanochannels.

The bubble initiation time is not affected by the length of the Pt patch at constant diffusion length and H_2O_2 concentration (Fig. 6). This confirms that the diffusion is the rate limiting step, since in a kinetically limited system, longer Pt lengths would lead to higher reaction rates and thus, faster bubble nucleation times. Only the smallest Pt patches (35 μm) in the experiment with 0.64 mole H_2O_2 per L (Fig. 6a) show slightly longer bubble initiation time, probably due to incomplete H_2O_2 conversion and consequently H_2O_2 crossing-over of the Pt patch.

Model catalyst pore

The results presented in this work demonstrate that formation of bubbles in porous catalyst supports influences the apparent activity of the catalyst, based on visual observations. Surprisingly, both retardation and enhancement of the activity are observed.

Decreasing the apparent activity by blocking the access of the reactants to the catalytic active sites with bubbles is an effect that can intuitively be expected if the bubble covers the catalyst surface. Blockage can also occur if the bubble obstructs the pore by remaining between the reactants supply and the catalyst particles, causing isolation of the catalyst. This work provides evidence for this based on direct visual observation of local formation of O_2 bubbles in 1D pores. As practical catalyst supports usually have a tortuous 3D pore morphology, this cannot be directly translated to practical catalysts. However, some supports do present similar 1D/2D pore-structures, *e.g.* mesoporous silicas, or contain dead-end pores like in activated carbon. It is reasonable to assume that the phenomena reported here could be relevant in such practical cases. Clearly, further work is required to prove this.

The observation that the reaction rate can also be enhanced thanks to bubble formation is in agreement with the oscillation theory described by Datsevich.[10] However, the mechanism proposed differs from the mechanism occurring

in our study. As explained in the introduction, Datsevich suggested that once the growing bubble reaches the pore mouth, the pressure of the bubble will equilibrate with the pressure of the reactor and would drag new liquid inside the pore. However, we show here that convection inside the pore can be induced without bubbles escaping from the pore, based on direct microscopic observations. The Gibbs free-energy released during the reaction, responsible for the formation of gas bubbles with enhanced internal pressure (eqn (4)) in combination with local differences in hydrophilicity between the Pt and the nanochannel surfaces, induce bubble movement, which leads to liquid displacement and convection. Both mechanisms are likely to happen in a real catalyst pore and could in principle be used to enhance mass transport and reaction rates. However, this would require a significant effort regarding the design and preparation of such practical catalyst supports. For instance, bubble migration could be favoured by using supports that combine hydrophilic and hydrophobic zones,[23] or by developing catalyst supports containing conical pores that could induce bubble flow from small pores to larger pores, or towards the bulk liquid as described by Datsevich.

Up to date, conventional descriptions of liquid phase reactions have applied concepts like the Weisz–Prater criteria and the Thiele modulus to compare reaction rates to internal mass transport. In this work, it was demonstrated that liquid phase reactions producing gas bubbles cannot be described using these concepts because of both enhancing as well as retarding effects on the reaction rate due to the formation of bubbles within the pores. Further work is required to develop a model than can describe these reactions. The results obtained in this study can initiate a new research sub-domain within the field of catalytic engineering, aiming at improving internal mass transfer in supported heterogeneous catalysis, *via* pore morphology and wettability of the pore walls.

Conclusions

Formation of gas inside model catalyst pores featured in a glass chip resulted in bubble nucleation above the catalyst patch. The reaction rate decreases dramatically when the bubbles start growing in the direction of the H_2O_2 feed stream, almost suppressing the reaction completely. On the other hand, when the bubbles grow towards the opposite direction of the feed stream, a forced convective flow is created inside the pores, enhancing the reaction rate 1–2 orders of magnitude. Bubble nucleation occurs more rapidly in case of short diffusion distances and high H_2O_2 concentrations. Instead, an increase in Pt amount did not influence the nucleation time, indicating that the reaction is diffusion limited. These experiments provide direct microscopic evidence that reactions generating gas inside pores of supported catalyst cannot be described using the conventional Thiele/Zeldovich description. Future work should focus on smart design and preparation of catalyst pore structures in order to benefit from the effects of bubble formation.

Conflicts of interest

There are no conflicts to declare.

Acknowledgements

We thank ir. Rolf Postma for helping with submitting the manuscript.

Notes and references

1 A. Chakrabarti, M. E. Ford, D. Gregory, R. Hu, C. J. Keturakis, S. Lwin, Y. Tang, Z. Yang, M. Zhu, M. A. Bañares and I. E. Wachs, *Catal. Today*, 2017, **283**, 27–53.
2 B. M. Weckhuysen, *Chem. Commun.*, 2002, 97–110.
3 E. W. Thiele, *Ind. Eng. Chem. Res.*, 1939, **31**(7), 916–920.
4 Y. B. Zeldovich, *J. Phys. Chem.*, 1939, **13**, 163–166.
5 M. Averill, *van Santen and van Leeuwen Catalysis: an integrated approach*, 2nd edn, Elsevier, 2000, p. 582.
6 H. S. Fogler, *Elements of chemical reaction engineering*, 2006.
7 R. Klaewkla, M. Arend and W. F. Hoelderich, *A Review of Mass Transfer Controlling the Reaction Rate in Heterogeneous Catalytic Systems*, INTECHOpen Access Publisher, 2011.
8 P. A. Ramachandran and R. B. Chaudhari, *Three phase catalytic reactors*, New York, 1983.
9 B. Blümich, L. B. Datsevich, A. Jess, T. Oehmichen, X. Ren and S. Stapf, *Chem. Eng. J.*, 2007, **134**(1–3), 35–44.
10 L. B. Datsevich, *Catal. Today*, 2003, **79–80**, 341–348.
11 L. B. Datsevich, *Appl. Catal., A*, 2003, **247**(1), 101–111.
12 L. B. Datsevich, *Appl. Catal., A*, 2003, **250**(1), 125–141.
13 L. B. Datsevich, *Appl. Catal., A*, 2004, **262**(2), 149–153.
14 L. B. Datsevich, *Appl. Catal., A*, 2004, **273**(1–2), 151–156.
15 L. B. Datsevich, *Appl. Catal., A*, 2005, **279**(1–2), 181–185.
16 L. B. Datsevich, *Appl. Catal., A*, 2005, **294**(1), 22–33.
17 T. Oehmichen, L. Datsevich and A. Jess, *Chem. Eng. Technol.*, 2010, **33**(6), 921–931.
18 T. Oehmichen, L. Datsevich and A. Jess, *Chem. Eng. Technol.*, 2010, **33**(6), 911–920.
19 D. W. McKee, *J. Catal.*, 1969, **14**(4), 355–364.
20 L. Kreja, *Z. Phys. Chem.*, 1984, **140**, 247.
21 *CRC Handbook of Chemistry and Physics*, ed. W. M. Haynes, 2014.
22 R. Sander, *Atmos. Chem. Phys.*, 2015, **15**(8), 4399–4981.
23 C. Franch, R. G. H. Lammertink and L. Lefferts, *Appl. Catal., A*, 2014, **156–157**, 166–172.